

## Stable MoSi<sub>2</sub> nanofilms with controllable and high metallicity

Liang-Feng Huang and James M. Rondinelli\*

*Department of Materials Science and Engineering, Northwestern University, Evanston, Illinois 60208, USA*

(Received 2 August 2017; published 20 November 2017)

We use density functional theory calculations to show nanofilms of covalent MoSi<sub>2</sub> exhibit tunable carrier densities and high metallicity at the Fermi level. We determine the nanofilm stabilities by assessing their formation energies, surface energies, and phonon spectra. The dependence of metallicity on the nanofilm geometry is explained using surface-termination-induced electronic structure changes and confinement effects. Understanding this metallicity not only is important to further improve the oxidation resistance of related alloys, but also will facilitate the identification of various thin films of MoSi<sub>2</sub> alloys and should lead to their use in nanoelectronic, electrochemical catalysis and low-dimensional transport experiments.

DOI: [10.1103/PhysRevMaterials.1.063001](https://doi.org/10.1103/PhysRevMaterials.1.063001)

As the spatial dimension of a material decreases, its electronic states will deviate from those in the bulk; the electronic structure is also likely more sensitive to exterior perturbations. Intriguing low-dimensional phenomena include odd multiple-particle scattering in various low-dimensional systems [1], superconductivity in GaAs/AlGaAs heterojunctions [2] and Pb-based ultrathin films [3], the Kondo effect at conducting surfaces with magnetic adsorbates/defects [4], giant electric/magnetic-field-induced effects on transport properties of graphene [5], and the remarkable quantum-size stability effect on metallic ultrathin films [6,7]. Furthermore, low-dimensional electronic mechanisms may also be important in some industrial applications, e.g., the nanoscale components in integrated circuits [8] and the early-stage oxidation (oxide thickness  $\lesssim 10$  nm) of metal surfaces [9].

Therefore, investigating low-dimensional materials can facilitate both fundamental property insights and enable material optimization for targeted technologies. Indeed, two-dimensional graphene and transition-metal dichalcogenides [5,10], whose bulk counterparts have a long history of study and application in many fields, e.g., solid lubricant, battery, and catalysis, have spawned new materials for devices based on a few-atom-thick layers [11]. Less well studied nanomaterials include compounds of Mo-Si, which in bulk exhibit superior thermomechanic properties and oxidation resistance. Typically, Mo-Si alloys are used in high-temperature gas turbines [12], with MoSi<sub>2</sub> exhibiting the highest oxidation resistance—attributed to the SiO<sub>2</sub> outer layer that forms on the surface of the alloy. The oxidation resistance can also be tuned by B, Al, Nb, and Ti additions [13].

Here we use density functional theory (DFT) calculations to discern intrinsic pseudogaps in the electronic structure of the tetragonal and hexagonal bulk phases of MoSi<sub>2</sub>. These pseudogaps enable the tunable and high metallicity we find in MoSi<sub>2</sub> nanofilms, and we show that electronic properties originate from both surface and quantum-confinement effects. Formation energies, phonon spectra, and surface energies are further used to comprehensively demonstrate the nanofilms' stabilities. Owing to the tunable electronic properties, metallic MoSi<sub>2</sub> nanofilms should find use in nanoelectronic devices,

electrochemical catalysis, and studies in low-dimensional superconductivity.

MoSi<sub>2</sub> exhibits two common polymorphs: the tetragonal *C*11<sub>b</sub> (space group *I*4/*mmm*) and hexagonal *C*40 (*P*6<sub>2</sub>22) phases [14]. We construct MoSi<sub>2</sub> nanofilms based on the crystalline orientations observed in coatings and grain boundaries [15]: the nanofilms with (001) and (110) surfaces of the tetragonal (T) phase and the (0001) surface of the hexagonal (H) phase, which are denoted as T001, T110, and H0001 nanofilms, respectively. We consider MoSi<sub>2</sub> nanofilms with thicknesses (*h*) up to 7.2 nm, defined as the equimolar thickness [16]. The DFT calculations are performed using the Vienna *Ab Initio* Simulation Package [17] with the PBEsol functional [18], with modified electronic potential for both extended crystals and surfaces. The projector-augmented-wave method is used to describe the electronic wave functions and Hamiltonians with both efficiency and accuracy [19]. The phonon spectra are calculated using the small-displacement method [20] as implemented in the PHONOPY code package [21] with an atomic-displacement magnitude of 0.03 Å. Additional details for the nanofilm structures and computational method can be found in Ref. [22].

In addition to MoSi<sub>2</sub>, the silicides Mo<sub>3</sub>Si and Mo<sub>5</sub>Si<sub>3</sub> are observed in experiment [13]. According to their formation energies [*E<sub>f</sub>* per atom, Fig. 1(a)], where elemental Mo and Si are used as the calculation references, we identify that the thermodynamic stability of the alloy increases with Si content; MoSi<sub>2</sub> is the most stable. The metastable H-MoSi<sub>2</sub> is only slightly higher than that of the more stable T-MoSi<sub>2</sub> by 30.5 meV/atom. Such a chemical trend in thermodynamic stability is ascribed to the increased number of strong covalent Mo-Si bonds, which fully saturate in MoSi<sub>2</sub>. The covalency of MoSi<sub>2</sub> can be readily seen in the electronic density of states *g<sub>e</sub>* [Fig. 1(b)] and differential electronic density  $\Delta\rho$ , driven by interatomic bonding [Figs. 1(c) and 1(d)]. The interatomic bonding transfers electrons from the Mo and Si atoms ( $\Delta\rho < 0$ ) to the Mo-Si bonds ( $\Delta\rho > 0$ ), signifying the covalent bond character. The electronic bandwidth seen in the *g<sub>e</sub>* increases with increasing Si content, indicating the highly covalent Mo-Si interactions. Furthermore, the saturated covalency produces a pseudogap at the Fermi level in T-MoSi<sub>2</sub> and H-MoSi<sub>2</sub> [Fig. 1(b)], suggesting the possibility to realize a tunable electronic structure in MoSi<sub>2</sub> by changes in local structure and chemical bonding. This observation in bulk

\*jrondinelli@northwestern.edu

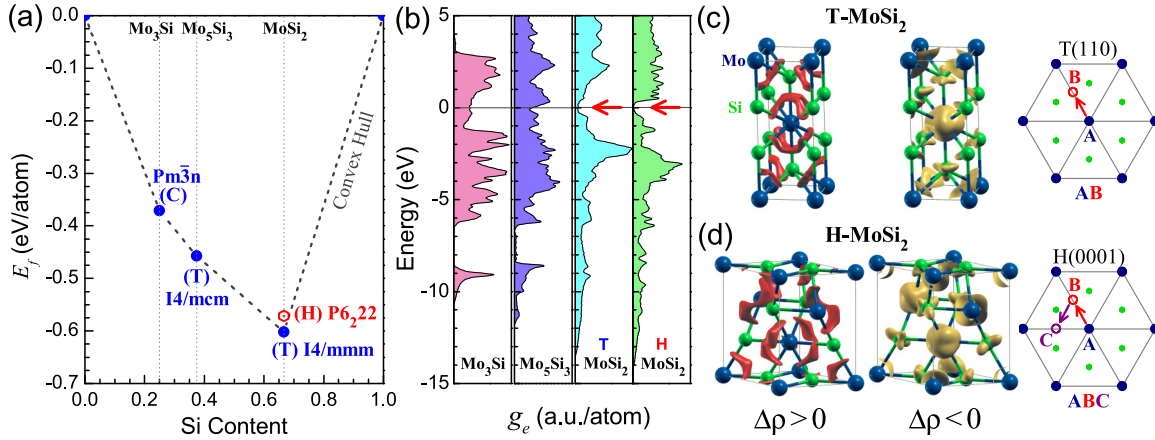


FIG. 1. (a, b) Formation energies and densities of states  $g_e$  for Mo-Si alloys. The Fermi level  $\varepsilon_F$  in (b) is at 0 eV and the arrow indicates the opening of a pseudogap. (c, d) The primitive cells of T- and H-MoSi<sub>2</sub> together with their differential electronic densities  $\Delta\rho$  (isovalue  $\pm 0.06 e/\text{\AA}^3$ ), and schematic structures of the T(110) and H(0001) planes. The AB and ABC stacking orders of the atomic layers are defined in (c, d), where the arrows indicate the lattice translations between neighboring planes.

MoSi<sub>2</sub> motivates us to investigate the evolution of its electronic properties in nanofilm geometries.

The T110 and H0001 MoSi<sub>2</sub> structures are comprised of interwoven Mo and Si sublattices [Figs. 1(c) and 1(d), right]. Both the T110 and H0001 structures when viewed along [110] and [0001], respectively, exhibit hexagonal bipartite lattices comprised of Mo and Si in a stoichiometric ratio, which is beneficial to the nanofilm stability (as described later). In bulk MoSi<sub>2</sub>, the T110 structure is generated through an AB stacking along [110] [Fig. 1(c)], whereas the H0001 structure exhibits an ABC stacking along [0001] [Fig. 1(d)]. The interaxial angle of the hexagonal (110) net in the T110 structure slightly deviates from the ideal hexagonal geometry ( $\theta = 120.03^\circ$  versus  $120^\circ$ ) in the H0001 structure owing to the lattice tetragonality in T-MoSi<sub>2</sub>. When T-MoSi<sub>2</sub> is viewed along  $\langle 001 \rangle$ , each Mo layer is sandwiched between two Si layers [Fig. 1(c), left]; therefore, we only consider T001 nanofilms with integer multiples of this MoSi<sub>2</sub> triple layer to maintain the most stable MoSi<sub>2</sub> stoichiometry.

We next assess the nanofilm stability by computing the formation energy [ $E_f$ , Fig. 2(a)], surface energy ( $\gamma$ , Table I), and phonon spectra [Fig. 2(b)]. The former two properties indicate the thermodynamic stabilities, whereas the latter indicates the dynamic stability. The calculated nanofilm formation energies per formula unit exhibit a linear relationship with inverse thickness  $1/h$  [Fig. 2(a)], especially for  $h > 0.8$  nm ( $1/h < 1.2 \text{ nm}^{-1}$ ), which can be described by

$$E_f(h) = E_f(\infty) + \frac{2A_s d_0 \gamma_0}{h}, \quad (1)$$

where  $E_f(\infty)$  is the bulk formation energy per formula unit,  $A_s$  is the nanofilm's unit-cell surface area,  $d_0$  is the thickness per MoSi<sub>2</sub> layer, and  $\gamma_0$  is the surface energy.

Figure 2(a) shows that all three nanofilms exhibit negative formation energies at  $h \gtrsim 0.7$  nm ( $1/h \lesssim 1.35 \text{ nm}^{-1}$ ), indicating the stability of MoSi<sub>2</sub> nanofilms against compositional segregation into elemental Mo and Si. Although bulk T-MoSi<sub>2</sub> has a lower formation energy than H-MoSi<sub>2</sub> [Fig. 1(a)], we find the H0001 nanofilm becomes more stable than the T001

and T110 nanofilms at  $h \lesssim 2.0$  and  $\lesssim 0.9$  nm, respectively. At  $h^{-1} = 0$ , the energies of the T001 and T110 nanofilms are degenerate while the T001-T110 energy difference increases with decreasing  $h$ .

The aforementioned stability variations with nanofilm thickness can be understood by considering the different surface energies (Table I): H0001 (T001) nanofilm has the lowest (highest)  $\gamma_0$ ; thus, its relative stability increases (decreases) with decreasing  $h$ . The intermediate  $\gamma_0$  for T110 makes the relative stability of its nanofilms with respect to T001 (H0001) nanofilm increase (decrease). The atomic layers in T110 and H0001 exhibit interwoven bipartite Mo-Si sublattices that do not disrupt the Mo-Si bonding when a cleaved surface is formed; however, the T001 nanofilm only has Si atoms on the surface [Figs. 1(c) and 1(d)], making the (001) surface the least favored (largest  $\gamma_0$ ). As noted, the T110 and H0001 structures are constructed from similar hexagonal motifs but with layers that stack in different orders [AB versus ABC, Figs. 1(c) and 1(d)]. Because the Mo-*spd* and Si-*sp* hybrid orbitals are highly directional, covalent bonding preferences should favor the former stacking order, as T-MoSi<sub>2</sub> has a lower formation energy [Fig. 1(a)]. Thus, the interlayer bonds in T-MoSi<sub>2</sub> should be stronger than those in H-MoSi<sub>2</sub>, resulting a higher cleavage energy (i.e.,  $\gamma_0$ ) for the T(110) surface than that of the H(0001) surface.

At finite temperatures, the DFT surface energies should include thermal effects from both electronic and vibrational excitations [23]. We find that the thermal correction  $\delta\gamma = \gamma_T - \gamma_0$  (see Ref. [22] for detailed formula and more data), where  $\gamma_T$  is the finite-temperature surface free energy, is only  $\lesssim 5\%$  at temperatures  $\lesssim 600$  K (Table I), indicating the feasibility to assess surface stability using either  $\gamma_0$  or  $\gamma_T$ . When the calculated  $\gamma_T$ 's of MoSi<sub>2</sub> at 300 K are compared to those of some prototypical materials, e.g., diamond ( $\gamma \lesssim 5.9 \text{ J/m}^2$ ), silicon ( $\gamma \lesssim 2.0 \text{ J/m}^2$ ), and germanium ( $\gamma \lesssim 1.7 \text{ J/m}^2$ ) [24], we find that MoSi<sub>2</sub> alloys have moderate surface energies, indicating that experimental synthesis of flat surfaces should be possible. Indeed, flat hexagonal MoSi<sub>2</sub> surfaces were prepared recently as a template to grow silicene sheets [25].

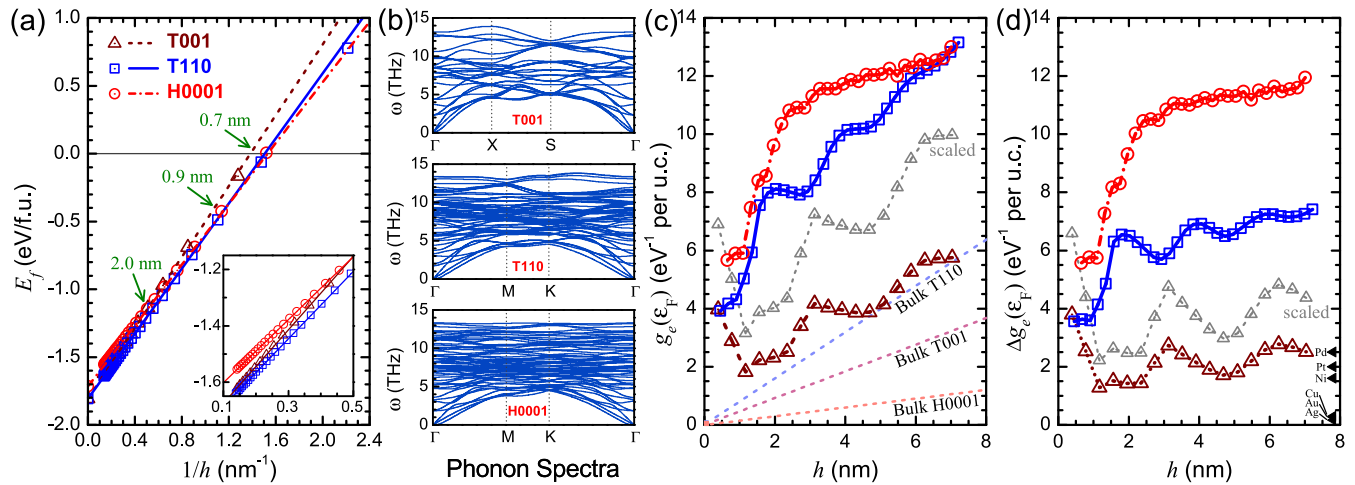


FIG. 2. (a) The formation energy versus inverse thickness ( $1/h$ ) for T001, T110, and H0001 nanofilms, where the symbols (lines) are the DFT data (fitted curves). The critical thickness for  $E_f < 0$  occurs at  $h = 0.7$  nm. The T110-to-H0001 transition at 0.9 nm and the T001-to-H0001 transition at 2.0 nm are indicated. The inset shows the energetics for  $2 \leq h \leq 10$  nm. (b) Phonon dispersion curves for the T001 (1.2 nm), T110 (1.3 nm), and H0001 (1.3 nm) nanofilms. (c, d) The variations in the total densities of states for the nanofilms and differences relative to the bulk materials at the Fermi level  $\Delta g_e(\epsilon_F)$  with thickness. Note that the T001 nanofilm data are also scaled by  $A_{T110}/A_{T001}$ , where  $A$  is the unit-cell surface area, to facilitate comparison.

Furthermore, substrate-supported Si nanofilms (thickness  $\gtrsim 1.4$  nm) [26] and freestanding Si nanowires (diameter  $\gtrsim 9$  nm) [27] have been widely fabricated. Owing to surface energies comparable to Si, we anticipate thin MoSi<sub>2</sub> nanofilms will soon be reported.

Apart from the favorable thermodynamic stabilities, we next assess the dynamical stability of the MoSi<sub>2</sub> nanofilms. The highly linear  $E_f - 1/h$  relationship at  $h \gtrsim 0.8$  nm indicates a negligible intersurface interaction effect on the energetics [Fig. 2(a)]; therefore, to study the lattice dynamics of an isolated surface, we select thin films with  $h \gtrsim 0.8$  nm, e.g., 1.2 ~ 1.3 nm (Fig. 2(b) and Ref. [22]). The absence of any imaginary modes in the phonon dispersions for all nanofilms confirms the stability of the films against spontaneous atomic reconstruction [Fig. 2(b)]. In addition, we find that the lowest acoustic mode for each nanofilm exhibits a quadratic dispersion,  $\omega \approx k^2$ , rather than the expected linear behavior upon approaching  $\Gamma$  (see Ref. [22]). Such quadratic acoustic phonons originate from the membrane effect intrinsic to low-dimensional systems [28] and has been found to be important in various lattice-dynamical properties of two-dimensional and layered materials [29]. Thus, we anticipate that the low-dimensional lattice-dynamical character will be enhanced by thinning the nanofilm, which is consistent with our calculated thickness-dependent MoSi<sub>2</sub> nanofilm phonon spectra [22].

TABLE I. Surface energies  $\gamma_0$  and  $\gamma_T$  (in J/m<sup>2</sup>) for T(001), T(110), and H(0001) surfaces of MoSi<sub>2</sub>. The former values are obtained by fitting the DFT data to Eq. (1).

	$\gamma_0$	$\gamma_T$ (0 K)	$\gamma_T$ (300 K)	$\gamma_T$ (600 K)
T(001)	2.626	2.591	2.553	2.486
T(110)	2.420	2.398	2.370	2.323
H(0001)	2.270	2.247	2.218	2.166

To understand the metallic nature of the nanofilms, we examine the electronic structure of the T001, T110, and H0001 nanofilms and bulk counterparts [Fig. 2(c)]. Note that because the T001 unit cell has a much smaller surface area (0.010 nm<sup>2</sup>) than the other two nanofilms' unit cells ( $\sim 0.018$  nm<sup>2</sup>), we scale the T001 density of states (DOS) at the Fermi level  $g_e(\epsilon_F)$  by a factor of 1.8 to facilitate the direct comparison among all nanofilms. Remarkably, all nanofilms exhibit significantly larger  $g_e(\epsilon_F)$  values than their corresponding bulk phases, indicating enhancement of the metallicity in the nanofilm geometry.

We next compute the difference between the nanofilm DOS at  $\epsilon_F$  and the bulk materials as  $\Delta g_e(\epsilon_F)$  to obtain the surface and quantum-confinement contributions to the electronic structure [Fig. 2(d)]. Solid triangular symbols in Fig. 2(d) represent the total  $g_e(\epsilon_F)$  values calculated for prototypical metal electrodes (Ni, Pd, Pt, Cu, Ag, and Au). First, we find that T001, T110, and H0001 exhibit quantitatively higher metallicity in the nanofilm geometry. The remarkable dependence of  $\Delta g_e(\epsilon_F)$  on nanofilm type and thickness suggests that the electronic properties may be readily tuned by changes to local structure. Next, we find the T001 and T110 nanofilms exhibit oscillations with wavelengths of approximately 3.2 and 2.0 nm, respectively, within the considered  $h$  range [Fig. 2(d)]. This behavior indicates a long-range Fabry-Pérot resonance from the confinement of the Fermi-level electronic states between the two nanofilm surfaces at  $h \approx m\pi/k_F$ , where  $k_F$  is the electronic-state wave vector and  $m$  is an integer (half-integer) for the in-phase (out-of-phase) resonance at the  $\Delta g_e(\epsilon_F)$  peaks (valleys).

To understand this oscillatory behavior, we examine the electronic band dispersions and the total and projected  $g_e$  spectra in detail [Figs. 3(a)–3(e)]. Projections are made onto the top ( $L1$ ) and subsurface ( $L2$ ) MoSi<sub>2</sub> layers and are compared to those for the center ( $Lc$ ) layer in Figs. 3(c)–3(e). Figures 3(c)–3(e) show that the electronic-subband

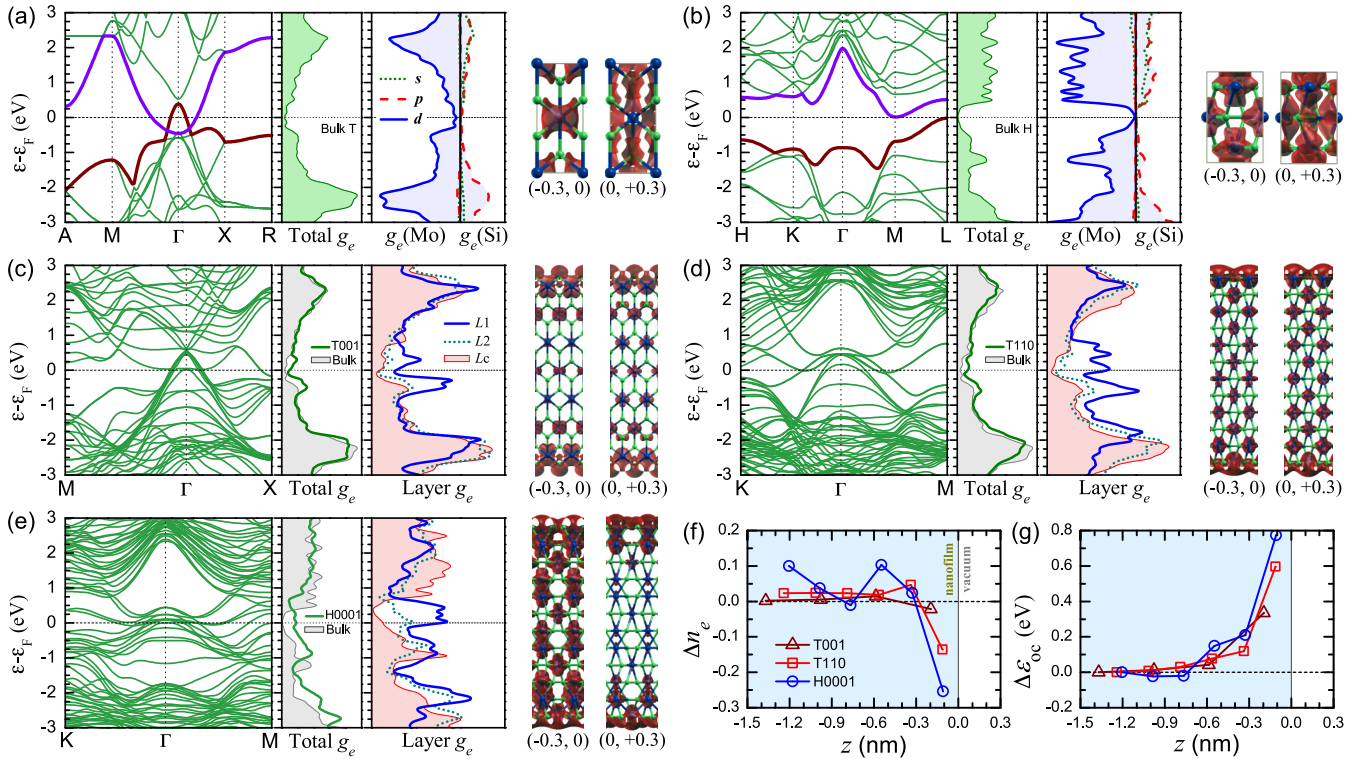


FIG. 3. (a)–(e) Electronic band dispersions, total densities of states  $g_e$ , projected  $g_e$  (for atomic orbitals or  $\text{MoSi}_2$  layers), and  $\rho_{\pm\epsilon_F}$  for bulk  $\text{MoSi}_2$  (T and H), T001 (2.74 nm), T110 (2.71 nm), and H0001 (2.63 nm) nanofilms. The plotted ranges for the total (a–e), orbital-projected (a, b), and layer-projected (c–e) DOS are  $[0, 5]$ ,  $[-4, 2]$ , and  $[0, 3]$   $\text{eV}^{-1}/\text{f.u.}$ , respectively, and the isovalue for  $\rho_{\pm\epsilon_F}$  is 5% of the maxima. Additional electronic structures are given in Ref. [22]. (f, g) The depth ( $z$ ) profiles for the electronic number ( $\Delta n_e$ , reference is the average  $n_e$ ) and occupation energy ( $\Delta\epsilon_{oc}$ , reference is the center-layer  $\epsilon_{oc}$ ) for  $\text{MoSi}_2$  layers in the nanofilms.

maxima/minima will touch (deviate from) the  $\epsilon_F$  at the in-phase (out-of-phase) resonances. However, such oscillation is absent in the H0001  $\Delta g_e(\epsilon_F)$  curve [Fig. 2(d)], because in the vicinity of both  $\Gamma$  and  $M$ ,  $\mathbf{k} = (\frac{1}{2}, 0, 0)$ , a reciprocal point with sixfold symmetry, there are many electronic bands with considerably different wave vectors crossing the Fermi level [Fig. 3(e)]; this superposition of multiple waves results in a monotonic  $\Delta g_e(\epsilon_F)$  curve.

We next explore the origin of the high metallicity by focusing on the spatial distribution of the low-energy electronic states near  $\epsilon_F$  and obtain the integrated charge density within two small energy windows defined as  $\rho_{-\epsilon_F} = [-0.3, 0.0]$  eV and  $\rho_{+\epsilon_F} = [0.0, +0.3]$  eV (Figs. 3(c)–3(e), right two panels). Major localization of these states occurs on the surface and extends to the inner two layers, as seen in the  $\rho_{-\epsilon_F}$  and  $\rho_{+\epsilon_F}$  projections; the homogeneous parts across the nanofilms arise from the bulk states. Next, we examine the penetration of the surface effect into the nanofilm by calculating the number of valence electrons as  $n_e = \int_0^{\epsilon_F} g_e d\epsilon$ , where the energy reference is given as the valence band edge and the occupation energy  $\epsilon_{oc} = \frac{1}{n_e} \int_0^{\epsilon_F} (\epsilon - \epsilon_F) g_e d\epsilon$  [30] for the  $\text{MoSi}_2$  layers [Figs. 3(f) and 3(g)]. Here we find that the surface effect has a significant contribution to the electronic structure, extending to a depth of  $2 \sim 3$   $\text{MoSi}_2$  layers ( $|z| = 0.4 \sim 0.6$  Å), which explains the diminishing inter-surface interaction at  $h \gtrsim 0.8$  nm, as deduced above from the thickness-dependent energetics. Note that the oscillating  $n_e(z)$  behavior in the H0001 nanofilm may be ascribed to the large confinement

effect therein, and similar charge-density oscillations are found in other metallic films [6].

By ranking  $\Delta g_e(\epsilon_F)$  in order of magnitude, we find H0001 > T110 > T001, which arises from two contributions: the aforementioned conducting surface electronic states and confinement-induced shifts in the electronic band energies. From the projected DOS of the L1 and L2  $\text{MoSi}_2$  layers in the different nanofilms [Figs. 3(c)–3(e)], we deduce that the number of conducting surface electrons follows the same trend, i.e., H(0001) > T(110) > T(001). For each nanofilm, we calculate the ratio of conducting surface electrons to the total metallicity as

$$r_s = \frac{2[g_e(L1) + g_e(L2) - 2g_e(Lc)]}{\sum_i g_e(Li)} \Big|_{\epsilon=\epsilon_F}, \quad (2)$$

and the obtained  $r_s$  values for the T001, T110, and H0001 nanofilms (at  $h \approx 2.7$  nm) of 40%, 63%, and 56%, respectively. From the relative positions between the pseudogap and  $\epsilon_F$  in the total DOS and the projected DOS for the Lc layer, we find that the band energies shift to higher energy in the same H0001 > T110 > T001 order due to quantum confinement. The reduced strength of the confinement effect is also reflected by the decreased delocalization observed in  $\rho_{-\epsilon_F}$  (for occupied states) upon moving from the H0001 to T110 and T001 nanofilms and is a direct consequence of the crystal chemistry of the T- and H- $\text{MoSi}_2$  phases. The bulk T- and H- $\text{MoSi}_2$  formation energies [Fig. 1(a)] and electronic structures [Figs. 3(a) and 3(b)] indicate that chemical bonds in T- $\text{MoSi}_2$  have higher

bonding strength and metallic character than those in H-MoSi<sub>2</sub>, resulting in higher resistance and larger electronic screening of the T-MoSi<sub>2</sub> bonds against surface perturbations. Therefore, both surface and confinement effects contribute to the high sensitivity of the metallicity on nanofilm type.

Based on covalent MoSi<sub>2</sub>, a structural alloy used for high-temperature applications, we proposed stable and highly metallic nanofilms that can be tuned by changes in crystal structure, crystalline orientation, and thickness. The metallic MoSi<sub>2</sub> nanofilms, as well as the metallicity mechanisms, may be useful in the characterization, design, and application of related materials. Raman spectroscopy has been used to characterize the formation of MoSi<sub>2</sub> films in multiple Mo-Si layers [31]. Bulk T-MoSi<sub>2</sub> is metallic, thus, there is no LO-TO splitting originating from the nonanalytical contributions in the dielectric response [32]. Bulk H-MoSi<sub>2</sub> has an optical band gap of  $\sim 0.5$  eV [Fig. 3(b)] and LO-TO splitting may be possible; however, high metallicity can be readily induced by various factors (e.g., finite size, surfaces, grain boundaries, and indirect-band-gap electronic excitation), which will likely quench the LO-TO splitting. See Ref. [22] for the detailed phonon spectra of T- and H-MoSi<sub>2</sub>.

During the early-stage oxidation of metals, the electric field established by the electrons transferred from the metal surface across the thin oxide film plays a decisive role [9], and this oxide film may act as a template for subsequent oxidation. Thus, the metallicity-enhancing mechanisms found here may

help in understanding and designing the oxidation resistance of MoSi<sub>2</sub> alloys. When a surface reactivity is sensitive to the number of available carriers, the tunable metallicity of MoSi<sub>2</sub> may find use in electrochemical catalysis applications.

The metallicity in low-dimensional MoSi<sub>2</sub> nanofilms may also enable intriguing fundamental physical properties. Superconductors have been found in various metallic systems with a high degree of covalent character, e.g., MgB<sub>2</sub> ( $T_c = 40$  K) [33], intercalated graphites (YbC<sub>6</sub> and CaC<sub>6</sub>,  $T_c = 6.5$  and 11.5 K) [34], and boron-doped diamond/silicon ( $T_c \lesssim 4$  K) [35]. In addition, an oscillating superconductivity has been found in Pb thin films [3]. Thus, we propose experimental studies of possible superconductivity in the covalent MoSi<sub>2</sub> nanofilms with high metallicity. The electronic screening (correlation) in conducting materials tends to decrease (increase) with decreasing geometric dimensionality, which could enable the giant Kondo effect that has been widely observed in low-dimensional conducting systems [36].

L.-F.H. and J.M.R. wish to thank Professor P. Reinke, Professor X. H. Zheng, and Professor Z. Zeng for the helpful discussions. This work was supported by the Office of Naval Research (ONR) (Contract No. N00014-16-1-2280). Calculations were performed using the QUEST HPC Facility at Northwestern, the HPCMP facilities at the Navy DSRC, and the CARBON Cluster at Argonne National Laboratory (DOE-BES, Contract No. DE-AC02-06CH11357).

- 
- [1] J. J. Lin and J. P. Bird, *J. Phys.: Condens. Matter* **14**, R501 (2002).
- [2] S. J. Bending, K. von Klitzing, and K. Ploog, *Phys. Rev. Lett.* **65**, 1060 (1990); *Phys. Rev. B* **42**, 9859 (1990).
- [3] Y. Guo, Y.-F. Zhang, X.-Y. Bao, T.-Z. Han, Z. Tang, L.-X. Zhang, W.-G. Zhu, E. G. Wang, Q. Niu, Z. Q. Qiu, J.-F. Jia, Z.-X. Zhao, and Q.-K. Xue, *Science* **306**, 1915 (2004); M. M. Özer, Y. Jia, Z. Zhang, J. R. Thompson, and H. H. Weitering, *ibid.* **316**, 1594 (2007); S. Qin, J. Kim, Q. Niu, and C.-K. Shih, *ibid.* **324**, 1314 (2009).
- [4] N. Knorr, M. A. Schneider, L. Diekhöner, P. Wahl, and K. Kern, *Phys. Rev. Lett.* **88**, 096804 (2002); A. Zhao, Q. Li, L. Chen, H. Xiang, W. Wang, S. Pan, B. Wang, X. Xiao, J. Yang, J. G. Hou, and Q. Zhu, *Science* **309**, 1542 (2005); J. Nygård, D. H. Cobden, and P. E. Lindelof, *Nature (London)* **408**, 342 (2000); J.-H. Chen, L. Li, W. G. Cullen, E. D. Williams, and M. S. Fuhrer, *Nat. Phys.* **7**, 535 (2011).
- [5] A. K. Geim and K. S. Novoselov, *Nat. Mater.* **6**, 183 (2007).
- [6] Z. Zhang, Q. Niu, and C.-K. Shih, *Phys. Rev. Lett.* **80**, 5381 (1998).
- [7] M. M. Özer, C.-Z. Wang, Z. Zhang, and H. H. Weitering, *J. Low Temp. Phys.* **157**, 221 (2009).
- [8] F. Schwierz, *Nat. Nanotechnol.* **5**, 487 (2010).
- [9] N. Cabrera and N. F. Mott, *Rep. Prog. Phys.* **12**, 163 (1949); A. Atkinson, *Rev. Mod. Phys.* **57**, 437 (1985); J. D. Baran, H. Grönbeck, and A. Hellman, *Phys. Rev. Lett.* **112**, 146103 (2014).
- [10] H. Ramakrishna-Matte, A. Gomathi, A. Manna, D. Late, R. Datta, S. Pati, and C. Rao, *Angew. Chem., Int. Ed.* **49**, 4059 (2010); V. Singh, D. Joung, L. Zhai, S. Das, S. I. Khondaker, and S. Seal, *Prog. Mater. Sci.* **56**, 1178 (2011); X. Huang, Z. Zeng, and H. Zhang, *Chem. Soc. Rev.* **42**, 1934 (2013).
- [11] D. Jariwala, T. J. Marks, and M. C. Hersam, *Nat. Mater.* **16**, 170 (2017).
- [12] J.-C. Zhao and J. H. Westbrook, *MRS Bull.* **28**, 622 (2003); D. M. Dimiduk and J. H. Perepezko, *ibid.* **28**, 639 (2003); J. H. Perepezko, *Science* **326**, 1068 (2009).
- [13] K. Ito, T. Murakami, K. Adachi, and M. Yamaguchi, *Intermetallics* **11**, 763 (2003); R. Sakidja, J. S. Park, J. Hamann, and J. H. Perepezko, *Scr. Mater.* **53**, 723 (2005); R. Sakidja, J. H. Perepezko, S. Kim, and N. Sekido, *Acta Mater.* **56**, 5223 (2008); J. S. Park, J. M. Kim, H. Y. Kim, S. Yi, and J. H. Perepezko, *Met. Mater.-Int.* **14**, 1 (2008); S. Majumdar and I. G. Sharma, *Intermetallics* **19**, 541 (2011); S. Majumdar, *Surf. Coat. Technol.* **206**, 3393 (2012); M. Azimovna Azim, S. Burk, B. Gorr, H.-J. Christ, D. Schliephake, M. Heilmair, R. Bornemann, and P. H. Bolívar, *Oxid. Met.* **80**, 231 (2013).
- [14] F. Nava, K. N. Tu, O. Thomas, J. P. Senateur, R. Madar, A. Borghesi, G. Guizzetti, U. Gottlieb, O. Laborde, and O. Bisi, *Mater. Sci. Rep.* **9**, 141 (1993); A. Belsky, M. Hellenbrandt, V. L. Karen, and P. Luksch, *Acta Crystallogr. Sect. B* **58**, 364 (2002).
- [15] K. Ito, T. Hayashi, M. Yokobayashi, and H. Numakura, *Intermetallics* **12**, 407 (2004); T. Yamazaki, Y. Koizumi, K. Yuge, A. Chiba, K. Hagihara, T. Nakano, K. Kishida, and H. Inui, *ibid.* **54**, 232 (2014).
- [16] L. D. Marks and L. Peng, *J. Phys.: Condens. Matter* **28**, 053001 (2016).

- [17] J. Hafner, *J. Comput. Chem.* **29**, 2044 (2008).
- [18] J. P. Perdew, A. Ruzsinszky, G. I. Csonka, O. A. Vydrov, G. E. Scuseria, L. A. Constantin, X. Zhou, and K. Burke, *Phys. Rev. Lett.* **100**, 136406 (2008); **102**, 039902(E) (2009).
- [19] P. E. Blöchl, *Phys. Rev. B* **50**, 17953 (1994); G. Kresse and D. Joubert, *ibid.* **59**, 1758 (1999).
- [20] G. Kresse, J. Furthmüller, and J. Hafner, *Europhys. Lett.* **32**, 729 (1995); K. Parlinski, Z. Q. Li, and Y. Kawazoe, *Phys. Rev. Lett.* **78**, 4063 (1997).
- [21] A. Togo and I. Tanaka, *Scr. Mater.* **108**, 1 (2015).
- [22] See Supplemental Material at <http://link.aps.org/supplemental/10.1103/PhysRevMaterials.1.063001> for auxiliary methodology details, structural information, phonon spectra for nanofilm and bulk forms of MoSi<sub>2</sub>, temperature-dependent surface free energies, and electronic structures.
- [23] L.-F. Huang, X.-Z. Lu, E. Tennesen, and J. M. Rondinelli, *Comput. Mater. Sci.* **120**, 84 (2016).
- [24] A. A. Stekolnikov and F. Bechstedt, *Phys. Rev. B* **72**, 125326 (2005).
- [25] C. Volders, E. Monazami, G. Ramalingam, and P. Reinke, *Nano Lett.* **17**, 299 (2017).
- [26] I. Aberg and J. L. Hoyt, *IEEE Electron Device Lett.* **26**, 661 (2005); E. Lioudakis and A. Othonos, *Phys. Status Solidi (RRL)* **2**, 19 (2008); V. Kulikovskiy, V. Vorlíček, P. Boháč, M. Stranyánek, R. Čtvrtlík, and A. Kurdyumov, *Thin Solid Films* **516**, 5368 (2008).
- [27] D. Li, Y. Wu, P. Kim, L. Shi, P. Yang, and A. Majumdar, *Appl. Phys. Lett.* **83**, 2934 (2003); D. M. Tang, C. L. Ren, M. S. Wang, X. Wei, N. Kawamoto, C. Liu, Y. Bando, M. Mitome, N. Fukata, and D. Golberg, *Nano Lett.* **12**, 1898 (2012).
- [28] I. M. Lifshitz, *Zh. Eksp. Teor. Fiz.* **22**, 475 (1952).
- [29] N. Mounet and N. Marzari, *Phys. Rev. B* **71**, 205214 (2005); L.-F. Huang and Z. Zeng, *J. Phys. Chem. C* **119**, 18779 (2015); L.-F. Huang, X.-Z. Lu, and J. M. Rondinelli, *Phys. Rev. Lett.* **117**, 115901 (2016).
- [30] H. L. Skriver, *Phys. Rev. B* **31**, 1909 (1985).
- [31] D. D. Allred, M. Cai, Q. Wang, D. M. Hatch, and A. Reyes-Mena, *J. X-Ray Sci. Technol.* **3**, 222 (1992); M. Cai, D. D. Allred, and A. Reyes-Mena, *J. Vac. Sci. Technol. A* **12**, 1535 (1994).
- [32] S. Baroni, S. De Gironcoli, A. Dal Corso, and P. Giannozzi, *Rev. Mod. Phys.* **73**, 515 (2001).
- [33] J. Kortus, I. I. Mazin, K. D. Belashchenko, V. P. Antropov, and L. L. Boyer, *Phys. Rev. Lett.* **86**, 4656 (2001); H. J. Choi, D. Roundy, H. Sun, M. L. Cohen, and S. G. Louie, *Nature (London)* **418**, 758 (2002).
- [34] T. E. Weller, M. Ellerby, S. S. Saxena, R. P. Smith, and N. T. Skipper, *Nat. Phys.* **1**, 39 (2005); I. I. Mazin, *Phys. Rev. Lett.* **95**, 227001 (2005); M. Calandra and F. Mauri, *ibid.* **95**, 237002 (2005).
- [35] E. A. Ekimov, V. A. Sidorov, E. D. Bauer, N. N. Mel'Nik, N. J. Curro, J. D. Thompson, and S. M. Stishov, *Nature (London)* **428**, 542 (2004); X. Blase, C. Adessi, and D. Connétable, *Phys. Rev. Lett.* **93**, 237004 (2004); E. Bustarret, J. Kačmarčík, C. Marcenat, E. Gheeraert, C. Cytermann, J. Marcus, and T. Klein, *ibid.* **93**, 237005 (2004); E. Bustarret, C. Marcenat, P. Achatz, J. Kačmarčík, F. Lévy, A. Huxley, L. Ortéga, E. Bourgeois, X. Blase, D. Débarre, and J. Boulmer, *Nature (London)* **444**, 465 (2006).
- [36] C. Buzea and T. Yamashita, *Supercond. Sci. Technol.* **14**, R115 (2001).